Statistical tracing of turbulent magnetic fields in the optically thick interstellar medium

Bo Yang,[1,2]★ Jian-Fu Zhang,[2,3]★ Alex Lazarian[2,4]★ and José Renan de Medeiros[5]

[1]*Department of Physics and Astronomy, University of Missouri, Columbia, MO 65211, USA*
[2]*Astronomy Department, University of Wisconsin, Madison, WI 53711, USA*
[3]*Department of Physics, Xiangtan University, Xiangtan, Hunan 411105, China*
[4]*Korea Astronomy and Space Science Institute, Daejeon 34055, Republic of Korea*
[5]*Universidade Federal do Rio Grande do Norte, Departamento de Física, 59072-970 Natal, RN, Brazil*

ABSTRACT

Based on high-resolution 3D data cubes from a magnetohydrodynamic (MHD) turbulence simulation, we study how to reveal the direction of the magnetic field within the optically thick interstellar medium by using the velocity gradient technique (VGT), correlation function anisotropy (CFA), and principal component analysis of anisotropies (PCAA). Considering the CO molecular tracers as a tracing method for radiative transfer processes, we find that the VGT and CFA can successfully trace the orientation of mean magnetic fields, which is in good agreement with the low-resolution numerical results obtained in the case of an optically thin medium. Similar to the simulation of an optically thin ISM, our simulations show that PCCA is still unusable in optically thick media. The synergetic application of the VGT and CFA to high-resolution spectroscopic observations is expected to yield valuable information on the interstellar magnetic field.

Key words: MHD – radiative transfer – methods: numerical – ISM: structure.

1 INTRODUCTION

Evidence of turbulence has been found from observations of electron densities, spectral lines and synchrotron fluctuations (e.g. Larson 1981; Armstrong, Rickett & Spangler 1995; Chepurnov & Lazarian 2010; Larson 1981; Xu & Zhang 2016a, b, also see Elmegreen & Scalo 2004 and McKee & Ostriker 2007 for synchrotron reviews). Turbulent magnetic fields play a very important role in key astrophysical processes such as star formation (Mouschovias & Spitzer 1976; Mestel & Spitzer 1956; Galli & Shu 1993; Padoan et al. 2006; Vázquez-Semadeni et al. 2011; Myers & Lazarian 1998; Burkhart et al. 2013; Xu & Lazarian 2020), the propagation and acceleration of cosmic rays (Fermi 1949; Schleicher et al. 2010; Chandran 2000; Yan & Lazarian 2002, 2008; Xu & Lazarian 2020), and the transfer of heat and mass in the galaxy (Narayan & Medvedev 2001; Lazarian 2006; Galli & Shu 1993; Green 1993; Deshpande, Dwarakanath & Goss 2000; Lazarian & Pogosyan 2004, 2006; Dickey et al. 2001; Khalil et al. 2006; Begum et al. 2006; Padoan et al. 2006; and see also Draine 2009 for a list of the phases). Therefore, obtaining the properties of magnetic turbulence is crucial for understanding the astrophysical processes involved in magnetic turbulence. The study of the turbulent magnetic field is so complicated that it might be constructive to find new ways to gain insight into the morphology of the magnetic field.

The interstellar medium (ISM) is turbulent and magnetized (Draine 2009; Burkhart et al. 2010; Federrath et al. 2011; Vázquez-Semadeni et al. 2011), on scales ranging from kiloparsecs to sub-astronomical units (Elmegreen & Scalo 2004), and is the place where turbulence is omnipresent. Based on the fact that the turbulent eddies in magnetized turbulence are anisotropic, with the elongated structure along the magnetic field direction (see Goldreich & Sridhar 1995, hereafter GS95), several magnetic field tracing techniques have been developed considering turbulent reconnection (see Lazarian & Vishniac 1999, hereafter LV99), which allows turbulent eddies to mix matter without a magnetic back-reaction.

There are several techniques to study magnetic field anisotropy. The first discussion of the possibility of studying anisotropy based on the properties of MHD turbulence was that of Lazarian, Pogosyan & Esquivel (2002). This resulted in the correlation function anisotropy (CFA) technique (see Esquivel & Lazarian 2005, 2011). The same idea, but realized not with correlation functions but by applying principal component analysis to the data, was implemented in the principal component analysis of anisotropies (PCAA, Brunt & Heyer 2002a, b; Heyer et al. 2008) technique. More recently, a more sophisticated technique that uses subtler properties of MHD turbulence, namely the velocity gradient technique (VGT, González-Casanova & Lazarian 2017; Lazarian et al. 2018), has been developed. Based on MHD turbulence data cubes, these three techniques were compared in Yuen et al. (2018) in the absence of self-absorption. There it was established that the VGT has advantages over the CFA and PCAA in tracing magnetic fields. The former is currently an intensely studied technique for tracing the direction and strength of magnetic fields (González-Casanova & Lazarian 2017; Lazarian et al. 2018; Hu, Yuen & Lazarian 2018).

★ E-mail: byang45@wisc.edu (By); jfzhang@xtu.edu.cn (J-FZ); alazarian@facstaff.wisc.edu (AL)

More importantly, it is essential to know the effects of absorption for most of the molecular lines used to study molecular clouds, and in particular for CO lines. In order to correctly understand and predict astrophysical phenomena, it is necessary to consider the absorption process due to radiative transfer that occurs in astrophysics. Magnetic field measurements involved in the optically thick ISM turbulence are essential for studying multiphase ISM properties. Using the line-emission detection method, Hsieh et al. (2019) and Hu et al. (2019) considered the effect of radiative transfer on the VGT measurement performance. They showed that the VGT is robust to tracing magnetic fields in the diffuse ISM and self-gravitating molecular clouds.

Dust polarization methods have commonly had certain limitations for the study of magnetic fields (Seifried et al. 2019). The depolarization is caused by intense variations in the magnetic field direction along the line of sight owing to turbulent motions. In addition, starlight polarimetry is limited by the lines of sight along which stars are present. Far-infrared polarization requires expensive missions, and thus the data are limited. Emission lines of molecular tracers are readily available, which significantly extends the opportunity to investigate magnetic fields.

We are currently considering the VGT as a powerful tool with which to study magnetic fields when there is no polarimetry or insufficient-resolution polarimetry. The VGT can make use of the Galactic rotation curve to study magnetic fields in molecular clouds (e.g. González-Casanova & Lazarian 2019) when the polarimetry cannot provide accurate measure owing to the line-of-sight confusion effect. Furthermore, by utilizing this tool, we can also study the magnetic fields at different optical depths of molecular clouds or in different phases of the ISM in both high- and low-frequency dust polarization owing to the limitations of dust polarization in the low-frequency domain.

Focusing on the case of an optically thick ISM, we use MHD turbulence simulation data cubes with the line-emission method of different molecular tracers to study the effect of radiative transfer on magnetic field measurement techniques. It is unknown whether the low-resolution numerical results mentioned above can be maintained when the numerical resolution is increased. In this paper, using higher-resolution data, we want to explore how the different optical depths of molecular tracers affect the performance of the VGT, CFA and PCAA methods in tracing magnetic fields, and to determine whether these techniques can be implemented together to measure the direction of the magnetic field within the optically thick ISM.

This paper is organized as follows. We introduce the theoretical foundation of MHD turbulence in Section 2, and the basis of three techniques tracing the magnetic field in Section 3. Section 4 describes the recipes for processing the MHD simulation 3D data to obtain the data, including the molecular tracer. We present the numerical results in Section 5, and provide a discussion and conclusion in Sections 6 and 7, respectively.

2 THEORETICAL FOUNDATION OF MAGNETIC FIELD MEASUREMENT

2.1 MHD turbulence theory

The magnetic field plays a crucial role in the dynamics of interstellar turbulence and makes the turbulent cascade anisotropic (Montgomery 1982; Higdon 1984). A significant advance in MHD turbulence theory was the discovery of quantitative anisotropic relationships between the parallel ($l_\parallel$) and perpendicular ($l_\perp$) scales of the eddies (GS95):

$$l_\parallel \propto l_\perp^{2/3}, \tag{1}$$

for a strong trans-Alfvénic (Mach number of $M_A \sim 1$) incompressible turbulence. A caveat here is that the GS95 relations between the parallel and perpendicular scales of the eddies were formulated in the frame of the projected mean magnetic field, for example the observer's frame. This would suggest a scale dependence of the magnetic field fluctuations observed in the interstellar media. This prompted some authors to search for such a scale-dependent anisotropy using spectroscopic and other forms of data (see Brunt & Heyer 2002a, b; Heyer et al. 2008).

The problem is that the correct formulation of MHD turbulence theory is only in terms of eddies elongated with the *local* magnetic field around these eddies. This formulation follows naturally as the consequence of the turbulent reconnection that makes such eddies possible (LV99). The concept of a *local* scale-dependent anisotropy is the cornerstone of the current understanding of MHD turbulence. This concept was numerically confirmed by Cho & Vishniac (2000), Maron & Goldreich (2001) and Cho & Lazarian (2002). The local direction of the magnetic field can be defined via the analysis of 3D numerical data cubes. For observational data, this is not possible. As an example, the measurements of the magnetic field orientation from dust polarization maps and velocity-channel data are projected measures on the plane of the sky, and are defined as line-of-sight averages relative to the observer's frame of reference, where no scale-dependent anisotropy exists, and the largest turbulent eddies determine the anisotropy at the injection scale. These turbulent eddies reflect the Alfvén Mach number at the injection scale L_{inj}; that is, $M_A = \delta B/B_0$, where B_0 is the mean magnetic field and δB is the magnetic field fluctuation. This can also be equivalently presented as $M_A = V_{inj}/V_A$, where V_{inj} is the turbulent injection velocity at L_{inj} and V_A is the Alfvén velocity. The GS95 was formulated for $M_A \equiv 1$ and later was generalized to both $M_A < 1$ and $M_A > 1$ in LV99 (see also Lazarian 2006).

Compressibility makes the turbulence more complicated (see Lithwick & Goldreich 2001). Cho & Lazarian (2002) demonstrated that fluctuations of the Alfvén and slow modes for both the velocity and the magnetic field maintain a similar relationship that is power-law: $E_k \sim k - 5/3$, while fluctuations of density obey a different scaling (see also Kowal & Lazarian 2010).

2.2 Velocity gradients

While the observations, as we discussed above, reveal only the global anisotropy, the eddies aligned with respect to the local system of reference are the key factor for the VGT. Because of that, the VGT, similar to the polarimetry, samples the magnetic field averaged along the line of sight, reflecting the real structure of the underlying magnetic field.

As a result of fast turbulent reconnection, the eddy cascade perpendicular to the local magnetic field is of Kolmogorov type; that is, with the turbulent velocity of the eddy $v_l \sim l_\perp^{-1/3}$, where $l_\perp$ is the scale of the eddy in the direction perpendicular to the local magnetic field direction. Therefore the velocity gradients scale as $v_l/l_\perp \sim l_\perp^{-2/3}$, meaning that the smallest resolved eddies induce the largest gradients. In practice, we adopt 90°-rotated velocity gradients to trace the magnetic field.

3 DESCRIPTION OF MEASUREMENT METHODS

3.1 Measuring velocity gradients

The VGT is suitable for analysing the position–position–velocity (PPV) data cube that can be obtained using the SPARX code (see Section 4). With PPV data cubes, we can calculate the velocity centroid and intensity, which are given by

$$C(x, y) = \frac{\int dv \, \rho(x, y, v) \, v}{I(x, y)}, \tag{2}$$

$$I(x, y) = \int dv \, \rho(x, y, v), \tag{3}$$

where ρ is the gas density and v is the velocity component along the line of sight. Equations (2) and (3) show that the centroid and intensity 2D maps are produced by integrating along the direction of that velocity axis of the PPV cube. A PPV cube is a 3D array with size n_x, n_y, n_v, where n_x and n_y represent the spatial resolution along the x- and y-axes, and n_v represents the number of velocity channels along the spectral line direction. The adjustable parameter n_v is set as $n_v = 200$ in this paper.

From the perspective of observation, the gradient measurement is the direct analysis of 2D data. For an arbitrary function $f(x, y)$, its gradient angle at pixel (x_i, y_j) is written as

$$\varphi_{i,j} = \tan^{-1} \left[\frac{f(x_i, y_{j+1}) - f(x_i, y_j)}{f(x_{i+1}, y_j) - f(x_i, y_j)} \right], \tag{4}$$

where $f(x, y)$ is $C(x, y)$ for the case of the velocity gradient and $I(x, y)$ for the case of intensity gradients (see Hu et al. 2019).

3.2 Correlation function anisotropy

In order to describe the spatial correlation of the eddies, the second-order correlation function of a velocity centroid map is defined as

$$CF(\mathbf{R}) = \langle C(r)C(r + \mathbf{R}) \rangle, \tag{5}$$

where $\langle ... \rangle$ denotes a spatial average over the map. The direction of the major axis of the eddies determines the orientation of the mean magnetic field in a sampled region (Esquivel & Lazarian 2011; Burkhart et al. 2014). In the case of a periodic boundary condition, it is easy to obtain the correlation function through the cross-correlation theorem and the fast Fourier transform (FFT):

$$CF(\mathbf{R}) = \mathfrak{F}^{-1}\{|\mathfrak{F}\{C\}|^2\}, \tag{6}$$

where $\mathfrak{F}$ is the Fourier transform operator.

The CFA of the centroid map and velocity channel demonstrated that the velocity anisotropies could reveal the direction of the mean magnetic field (Lazarian et al. 2002; Esquivel & Lazarian 2011; Esquivel, Lazarian & Pogosyan 2015). Furthermore, the CFA technique showed promise for determining the magnetization of the ISM (Esquivel & Lazarian 2011; Esquivel et al. 2015). The anisotropies revealed by the CFA were shown to be different for the Alfvén, slow and fast modes in the compressible MHD turbulence (see Kandel, Lazarian & Pogosyan 2016 for more details).

3.3 Principal component analysis of anisotropy

PCA is another way to analyse the velocity data cubes (Brunt & Heyer 2002a,b; Heyer et al. 2008). The physical basis is fundamental of extracting information from the PCA is closely associated with the turbulence velocity dispersion v^2. According to the GS95 scaling,

the larger eigenvalues correspond to the largest-scale contributions of turbulence eddies along the line of sight, $v^2 \sim (l^{1/3})^2 \sim l^{2/3}$, and this approach is used to separate the contributions of eddies of different sizes.

The anisotropy of turbulent velocities can also be revealed. The corresponding PCAA approach was introduced by Heyer et al. (2008). The fundamental idea of PCAA is that a map with a size of N can be mathematically represented by a series of eigenmaps; the magnetic field anisotropy can then be revealed through statistical calculations with these eigenmaps. The prediction of the magnetic field based on the anisotropy can be made by finding the characteristic velocity and scales in the turbulence. The orientation of the PCAA anisotropy direction at pixel position (i, j) can be calculated by

$$\vartheta_{i,j} = \tan^{-1} \left[\frac{\delta v_y L_x}{\delta v_x L_y} \right], \tag{7}$$

where $\delta v_{x, y}$ represents the characteristic velocity and $L_{x, y}$ stands for the characteristic scale obtained from the autocorrelated function associated with the eigenmaps extracted in the PCA procedure.

3.4 Subblock averaging and Hockney's method

We use the subblock averaging method to explore the general performance of the VGT, CFA and PCAA. This method can provide the statistically most likely direction of the mean magnetic field within each subblock region (Yuen & Lazarian 2017a) or part of the mosaic in practical observations. Because the gradient orientation distribution is Gaussian, the peak value could represent the averaged direction of gradients inside a selected block of the desired size. Thus, the averaged value of the maximum velocity gradient for each block can provide anisotropic eddy information.

Owing to the non-periodicity of boundaries for each subblock, we adopt Hockney's method (Hockney 1968) to carry out the computation of the correlation function, in which the open-boundary correlation function is written as

$$CF_C(\mathbf{R})[i, j] = \mathfrak{F}^{-1}\{\mathfrak{F}\{X\}\mathfrak{F}\{Y\}^*\}, \qquad 1 \le i, j \le n_x, \tag{8}$$

where n_x is the size of each subblock. Implementing this method would accelerate the computation of structure analysis, which benefits the result comparison between CFA and the VGT.

3.5 Alignment measure

In order to characterize the performance of the techniques we are studying, the directions of anisotropy/gradients are compared with the magnetic field direction from dust polarization emission. The latter is described by the Stokes parameters $Q(x, y)$ and $U(x, y)$, which are given by (Lee & Draine 1985, see also Lazarian 2007 and Andersson, Lazarian & Vaillancourt 2015 for reviews on grain alignment):

$$Q(x, y) \propto \int dz \rho(x, y, z) \cos[2\theta(x, y, z)],$$

$$U(x, y) \propto \int dz \rho(x, y, z) \sin[2\theta(x, y, z)], \tag{9}$$

where the angle θ can be calculated by $\tan \theta(x, y, z) = B_y(x, y, z)/B_x(x, y, z)$, in terms of the components (B_x and B_y) of the magnetic field along the x- and y-axes. Therefore, we have the dust polarization angle of $\Phi = 0.5 \arctan(U/Q)$. By defining a angle of ϕ between the magnetic field direction predicted by the three methods (VGT, CFA and PCAA) and that by the dust polarization angle, we use the

Table 1. Description of our MHD simulations. M_s and M_A are calculated using the snapshot data where the turbulence reaches a steady state. The resolution of all data is 792^3.

Run	M_s	M_A	$\beta = 2M_A^2/M_s^2$	$\delta B_{rms}/\langle B \rangle$
0	6.17	0.22	0.01	0.15
1	5.65	0.42	0.01	0.36
2	5.81	0.61	0.02	0.47
3	5.66	0.82	0.04	0.63
4	5.62	1.01	0.07	0.76
5	5.63	1.19	0.09	0.87
6	5.70	1.39	0.12	1.02
7	5.57	1.55	0.16	1.12
8	5.50	1.67	0.19	1.25
9	5.39	1.71	0.20	1.39

alignment measure (AM) of

$$AM = \langle 2\cos^2\phi - 1 \rangle \qquad (10)$$

to quantify the performance of specific magnetic field-tracing techniques (see González-Casanova & Lazarian 2017; Yuen & Lazarian 2017a).

4 NUMERICAL APPROACH

4.1 3D MHD turbulence data generation

Our high-resolution 792^3 data cubes are generated using the ZEUS-MP/3D code (Hayes et al. 2006), which deals with a single-fluid, operator-split, and staggered-grid MHD flow. In the ISM environment simulation, the initial injection of solenoidal turbulence and a periodic boundary condition are assumed, with a constraint of the equation of isothermal state. In the simulation, MHD turbulence is evolved long enough to reach a steady state, from which we extract the snapshot data, including the information on the 3D magnetic field, velocity and density. By changing the initial conditions, such as the injected energy and magnetic field strength, we obtain 10 different snapshot data, which simulate the multiphase ISM environment ranging from a strong turbulent region to a weak turbulent one. Each set of data cubes generated is characterized by the Alfvénic Mach number M_A and sonic Mach numbers M_s. Different running models listed in Table 1 represent the different possible ISMs ranging from sub-Alfvénic to super-Alfvénic regimes.

We emphasize that our purpose is to study the statistical tracing of turbulent magnetic fields in the optically thick ISM, without expecting to be involved in more complex physical processes. For applications to specific astrophysical settings, we should consider more factors, such as the self-gravity effect and the ambipolar diffusion process using the colliding flow approach (Chen & Ostriker 2014). We view turbulence in molecular clouds as part of the large turbulent cascade at the galactic scale. In addition, if we consider an isothermal condition and the molecular species (see next section), this can provide sufficient cooling in molecular clouds to make our simulations adequate.

4.2 Line-emission data generation

The presence of molecular species is implied as a molecular constituent of the gas within the MHD simulations. To obtain line-emission data from molecular species ^{12}CO, ^{13}CO and C^{18}O, we utilized the SPARX code (Simulation Package for Astronomical

Radiative Transfer, Xfer),[1] which has the capability to process MHD simulations of 3D data.

We used this software package to perform the local thermal equilibrium (LTE) radiative transfer computation by the line-emission method, assuming $T = 10$ K as the gas temperature of molecular clouds (Wilson, Walker & Thornley 1997), and 10 pc as the distance from the observer to the cloud. Numerically, SPARX reads the 3D data cubes we obtained in MHD simulations by ZEUS (indicating an optically thin ISM) to carry out the calculation of spectral line radiative transfer for three molecular transitions: ^{12}CO, ^{13}CO and C^{18}O. The abundance of these molecular isotopes satisfies the LTE thermal condition and they are dominant at different optical depths. Following the details provided in Hsieh et al. (2019), the fractional abundances of molecular species of the lowest transition (J = 1−0) ^{12}CO, ^{13}CO and C^{18}O are set as 1×10^{-4}, 2×10^{-6} and 1.7×10^{-7}, respectively. We obtained the SPARX-processed data cube, for example synthetic line-emission maps as a PPV data cube, including the molecular velocity and density in 200 velocity channels.

5 NUMERICAL RESULTS

When carrying out radiative transfer simulations with the SPARX code for each run presented in Table 1, we obtained different PPV data cubes for different molecular tracers. Using each PPV cube for CO isotopes, we computed the velocity centroid map and then applied the VGT, CFA and PCAA recipes to obtain the possible orientation of the magnetic field. In our calculation with the simulation pixel scale of 0.260 arcsec, we selected a field size of 88^2 pixels, or equivalently a field of view of 523.5 arcsec^2 for the subblock process, meaning that the subblock averaged angle is determined in the 88^2 pixel regime by the peak of the Gaussian fitting.

5.1 Velocity gradient techniques

In order to understand intuitively the measured magnetic field direction in each subblock, we show the distribution of the direction of the magnetic field in the left panel of Fig. 1, using the run2 data listed in Table 1. In this figure, the magnetic field directions predicted by the VGT (in blue) are compared with ones from the dust polarization method (in red) in each subblock regime. For the whole map, the value of the alignment measure is $AM = 0.67$ according to equation (10), which is an ideal alignment measure result because other factors are ignored in this technique, such as the spatial filtering of small-scale structures. We emphasize that when increasing the size of the subblock, we will obtain a slightly larger AM. A rigorous analysis of how changes in the block size affect the AM is given in previous works (Yuen & Lazarian 2017a; Yuen et al. 2018; Lazarian et al. 2018), and will not be discussed here.

The right panel of Fig. 1 presents the result from the synthetic line emission method of run2 data characterized by the ^{12}CO emission line. It can be seen that most subregions have better alignment, which results in a larger value of $AM = 0.92$. Compared with the measurement for the optically thin medium (left panel), the optically thick medium (right panel) with $\tau_{^{12}CO} = 21.65$ shows a better alignment measurement, which enhances the applicability of gradient techniques in the real self-absorbed interstellar environment. To understand the optical properties of three molecular species, we show in Fig. 2 the distribution of the average optical depth from
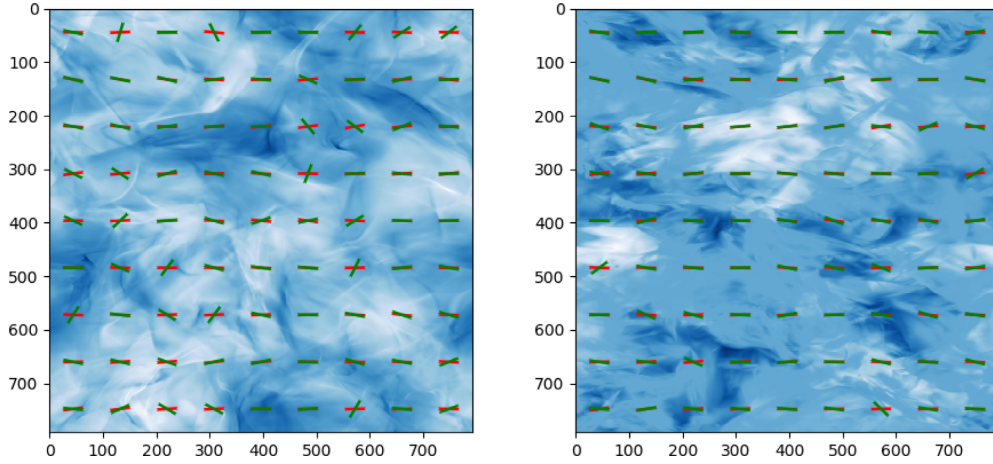
[1]**https://sparx.tiara.sinica.edu.tw/physics/**

Figure 1. Comparing magnetic field directions (in red) obtained by the dust polarization method with magnetic field directions predicted by the VGT. The results with $AM = 0.67$ (left panel) and 0.92 (right panel) are from the dust polarization method using run2 listed in Table 1 and the corresponding synthetic ^{12}CO line emission, respectively .
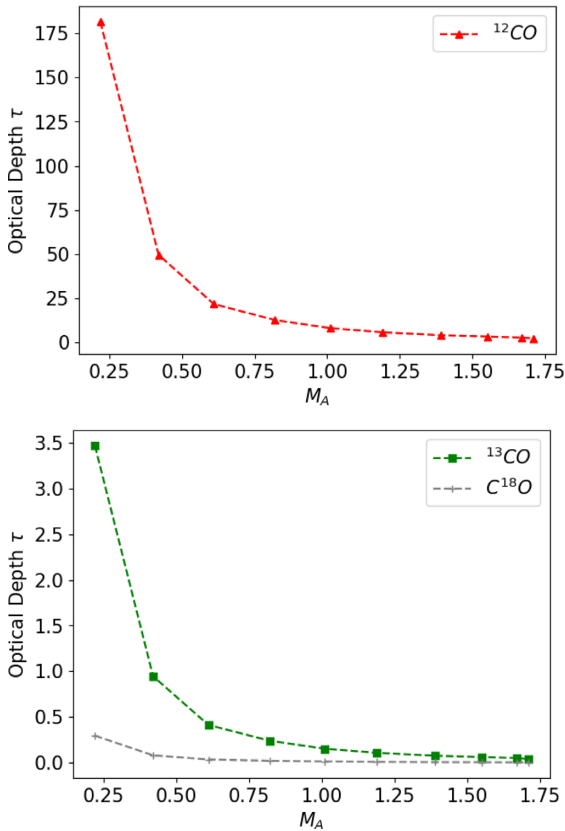

Figure 2. The average optical depth as a function of M_A for different molecular tracers ^{12}CO (upper panel), ^{13}CO and $C^{18}O$ (lower panel).

Figure 3. Alignment measures of the VGT using different molecular tracers, ^{12}CO, ^{13}CO and $C^{18}O$, compared with the results from the dust polarization measurement.

sub-Alfvénic to super-Alfvénic regimes. From this figure, it can be seen that with increasing M_A the optical depth decreases, and ^{12}CO as well as ^{13}CO are optically thick, while $C^{18}O$ is optically thin.

Next, we explore how the different molecular tracers affect the alignment measurement of the VGT. Fig. 3 presents the alignment measures of the VGT using different molecular tracers, ^{12}CO, ^{13}CO and $C^{18}O$, compared with the measurements of dust polarization. As shown in this figure, with increasing Alfvénic Mach number, all the AM values decrease, in particular in the super-Alfvénic turbulence regime. This result can be interpreted as follows: the motions at scales larger than $L_A = L_{in}M_A^{-3}$ are marginally affected by the magnetic field. Therefore the turbulence is essentially hydrodynamic-like (Lazarian 2006). However, at scales smaller than L_A, the gradient techniques are applicable. Technically, filtering the large-scale spatial structure can reveal the magnetic field structure in this regime (see Lazarian & Yuen 2018a; Zhang et al. 2019a). As shown in Fig. 3, consideration of the radiative transfer does not decrease the alignment of gradients and magnetic fields. The dust polarization measure has AMs somewhat smaller than those of the optically thick tracers ^{12}CO and optically thin tracers ^{13}CO.

The ability to trace the magnetic field by ^{12}CO molecules extends to the super-Alfvénic regime with $M_A \simeq 1.2$, where $\tau_{^{12}CO} \simeq 4$. Moreover, in the sub-Alfvénic regime case with ^{13}CO and $C^{18}O$, they share the same level uncertainty to trace magnetic field. The most significant difference between the CO molecular tracers in tracing the magnetic field is their optical depths. Although the nature of the effect requires further study, we might speculate that the distortions of the alignment arising from dense clumps are reduced because the clumps provide less contribution to the gradient signal. As a result,
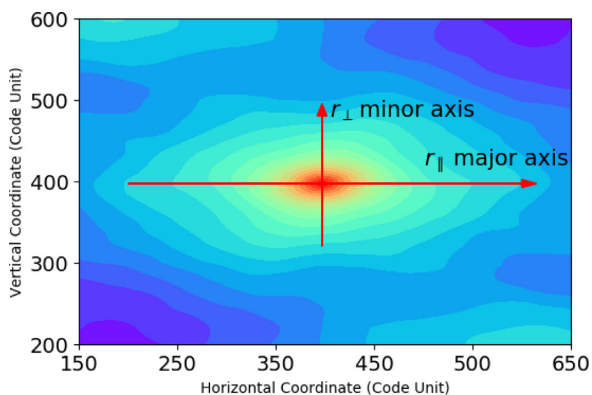
Figure 4. Illustration of the correlation function map of the velocity centroid obtained using the synthetic line-emission method run2 data of the ^{12}CO emission line. $r_\parallel$ and $r_\perp$ indicate the major and minor axes of elliptical contours, respectively. The centre of the ellipses coincides with the centre of map 792^2.

tracers ^{13}CO and C^{18}O can provide reliable alignment measures by the VGT in the sub-Alfvénic regime. As expected in observations, the abundance of CO isotopes is much lower than that of ^{12}CO, whose optical depth is higher than that of its isotopes (see Fig. 2). In our simulation, we sample the same spatial scale of magnetic turbulence along the line of sight because of our use of the constant number of 200 pixels of the velocity channel. Based on different optical depths of molecular tracers, we can sample different spatial depths along the line of sight; that is, ^{12}CO can trace the region close to the observer, while ^{13}CO and C^{18}O can sample the region farther from the observer.

5.2 Correlation function anisotropy

Fig. 4 illustrates a correlation function map of velocity centroids for the ^{12}CO emission line, obtained using the run2 data cube of the line-emission method. It can be seen that the anisotropic structure is elongated along the horizontal direction, forming a series of concentric ellipses centre of the correlation function map derived from the line-emission map. The major and minor axes of the elliptical contours are indicated by $r_\parallel$ and $r_\perp$, respectively. Owing to the periodic boundary condition used in the simulation, this result for the whole map is produced by the fast Fourier transformation method. With the anisotropy of MHD turbulence (GS95; LV99), we know that the mean magnetic field is parallel to the major axis $r_\parallel$ of ellipses, which makes it possible to trace the direction of the magnetic field by the correlation function analysis. Selecting a central region of an appropriate 30 pixels, we calculate the aspect ratio, which is the major to the minor axial ratio, to observe the level of anisotropy. Fig. 5 demonstrates the results for the aspect ratio as a function of the Alfvénic Mach number M_A. As M_A increases, the aspect ratio decreases, which indicates a reduced degree of anisotropy in the correlation function map of the velocity centroid. As can be seen from this figure, the anisotropy of the ^{12}CO molecule is the highest among all the molecules considered, suggesting that ^{12}CO can best trace the direction of the mean magnetic field.

However, the tracing of the magnetic field corresponds to each subregion has non-periodic characteristics because of boundary but the whole region of 792^2 has periodic characteristics. Therefore, we use Hockney's method (see Section 4) rather than the fast Fourier transformation method. With the method of line emission of the ^{12}CO molecule, the four subblock structures of correlation function maps
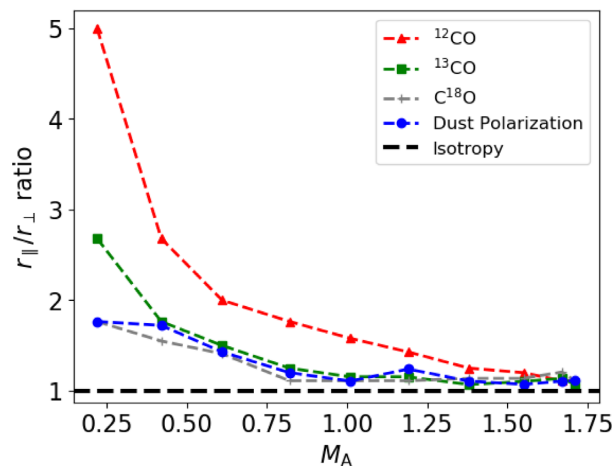

Figure 5. Ratio of the major axis ($r_\parallel$) of eddies to the minor axis ($r_\perp$) as a function of the Alfvénic Mach number M_A, calculated at a separation of $r = 30$ pixels from the centre (see Fig. 4).
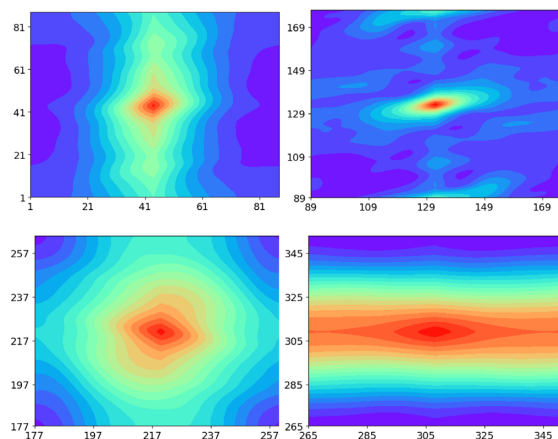

Figure 6. 2D images of the correlation function for four subblock regions with a size of 88 pixels. The results displayed are calculated using the open-boundary condition of the Hockney method and the run2 data of the line-emission method listed in Table 1 for the ^{12}CO emission line.

are shown in Fig. 6 as an example. For the map in each subblock regime, we can determine the major and minor axes of the concentric ellipse, the former of which constrains the direction of anisotropy, namely the direction of the local mean magnetic field. The map is then rotated such that the major axis of a contour with a particular radius (in this paper, we fix eight pixels for all simulations) is parallel to the horizontal direction, so that the resulting rotation angle is the orientation of the magnetic field to the horizontal axis. According to the above procedure, Fig. 7 provides the distribution of the measured magnetic field directions obtained using the ^{12}CO emission line. As is seen from the figure, CFA can indeed determine the direction of the mean magnetic field, with an ideal alignment measure of $AM = 0.59$ and $\tau_{^{12}CO} = 21.65$. As seen in the Fig. 8, we can notice the general AM performance of CFA for different CO isotopologues decreases as the optical depth decreases, which is in agreement with the general performance trend of the VGT.

5.3 Principal component analysis of anisotropy

According to the approach described previously, we plot in Fig. 9 the alignment measurement results of the PCAA, sampling the first N
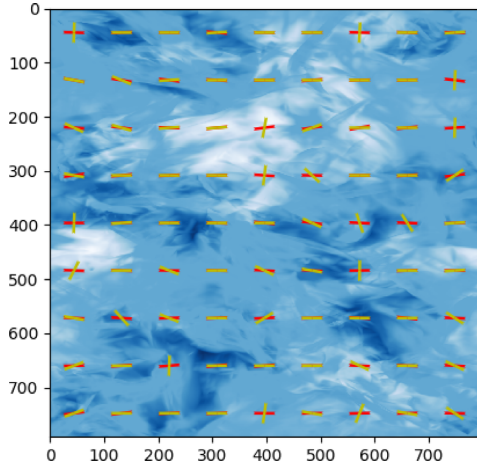
Figure 7. Illustration of magnetic field directions (red) calculated by the dust polarization method and magnetic field directions predicted by CFA of the ^{12}CO emission line. The obtained *AM* between them is 0.59 using run1 listed in Table 1.
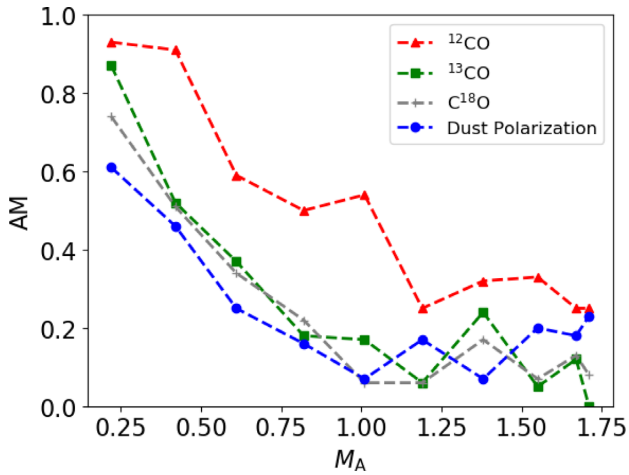

Figure 8. Alignment measures of CFA using different molecular tracers, ^{12}CO, ^{13}CO and C^{18}O, in comparison with results from the dust polarization method.
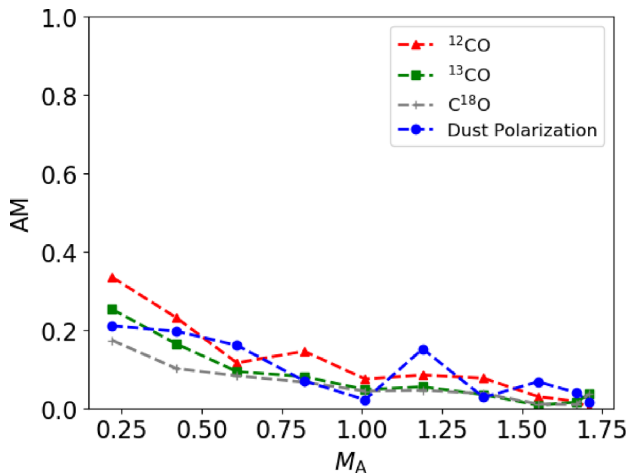

Figure 9. Alignment measures of PCAA using different molecular tracers, ^{12}CO, ^{13}CO and C^{18}O, compared with the method based on dust polarization measurements.

= 40 largest components of eigenvalues. We find that the alignment measures obtained by PCAA consistently show the inability of this method to trace the magnetic field. This means that the anisotropy analysis to obtain the eddies profiles from the PCA is inferior to the abilities demonstrated by the other two techniques in this paper. This result is in agreement with the earlier study in Yuen et al. (2018) obtained with numerical cubes without radiative transfer.

6 DISCUSSION

In general, using ^{12}CO and its isotopes ^{13}CO and C^{18}O as tracers of the eddy velocities, our studies demonstrate that the VGT and CFA can predict the direction of the mean magnetic field in optically thick or thin media. The CFA and VGT have the same performance trend with decreasing optical depth from sub- to super-Alfvénic regimes. Interestingly, the AM slope of the VGT is smaller than that of CFA. This implies that the VGT can potentially trace the magnetic field more reliably in optically thick media than can CFA. Even though PCAA cannot provide reliable tracing for the mean magnetic field, this technique can still provide insights into the reasonable magnetic field direction. Nevertheless, it is crucial to understand the limitations of these techniques, so that studying optically thick media with different molecular species can be meaningful for the observational community. With the integrated intensities versus the line-of-sight velocity distributions (see fig. 7 of Hsieh et al. 2019), we can understand the details of the techniques. Within the saturated (flat part of the intensity line profile) region, in which a constant pixel intensity spreads across the whole 200 channels with a small relative velocity, the performance of ^{12}CO might be hindered in probing the magnetic field of optically thick media. Because this region should only provide information from large-scale isotopic structures rather than from small-scale anisotropic ones where the gradient technique works effectively, there are insufficient gradient statistics. Therefore, the VGT mainly traces magnetic fields in high-velocity diffusion regions (two tails). As a result, the alignment measure in terms of the optically thick tracer ^{12}CO would perform better than that of optically thick ^{13}CO (changing to optically thin in a larger M_A regime) and optically thin C^{18}O.

When applying the VGT to observational data, note that the VGT is a technique based on an edge-detection algorithm to predict the direction of the local magnetic field. In general, the data resolution and quality determine the applicability and reliability for predicting the magnetic field direction and strength. The peak of gradient angle distributions fitted by Gaussian fitting will help us to determine the direction of the magnetic field within the subblock regime. In practice, the observational image and telescope beam size together determine the amount of velocity information that needed to predict the magnetic field. To fulfil the best measurement, improving the Gaussian fitting quality by increasing the number of measurements will be beneficial to obtain the velocity configuration in terms of the angle distribution. The block size of 88^2 used in this paper requires 88^2 instances of independent measurement or beam size, which corresponds to a region of 88^2 beam size in observations. The observation map and beam size ratio are necessary conditions for an observer to obtain reliable results.

Fissel et al. (2019) employed a relative alignment measure to study the cloud depth of different tracers, in which the full width at half-maximum (FWHM) of the Gaussian derivative kernel used to calculate the gradient angles is 45 arcsec and the FWHM resolution of Gaussian smoothed data cubes used to make the moment maps is 120 arcsec. In contrast, our work has the advantage of high resolution; that is, our simulation pixel scale is 0.260 arcsec, and

the subblock field is 88 pixels $\simeq$ 22.88 arcsec. The current research shows that our high-resolution results agree with the results of Fissel et al. (2019). Furthermore, the better performance of the VGT and CFA in the super-Alfvénic regime indicates the potential of the techniques. Even though the CFA or anisotropy study shows a somewhat inferior performance compared with the VGT, the CFA method can be employed to decompose compressible MHD turbulence into fundamental modes (e.g. Kandel et al. 2016).

Even though some scale parameters such as small block size and low numerical resolution could result in the visual distortion of the correlation function map and impede the magnetic field measurement, we note that in the case of high numerical resolution, the ability of CFA to trace the magnetic field is not affected. In the trans-Alfvénic regime, the CFA with ^{13}CO or its isotopes has the potential to determine the mean magnetic field direction, so that small-scale anisotropy can be better resolved. We noticed that the strip-like structure of the correlation function map result in an inability to trace the magnetic field by CFA, is mentioned in the previous study (Yuen et al. 2018); however, our high-resolution simulation can still obtain the orientation of meaning magnetic field within subblock regions, because a larger block size and higher resolution both can intrinsically filter out the small-scale noise-like structure. Therefore, for the smaller scale of the regime of interest, improving the resolution would be beneficial so that the correlation function map would correctly reveal the anisotropy of eddies. For the seemingly functional PCAA, our exploration showed its weak capability in tracing the magnetic field in higher-resolution data cubes, even though the previous study (Yuen et al. 2018) with lower-resolution data showed very limited good measurement in certain regions, which warrants further investigation of this potential technique. In this paper, compared with the mathematical simplicity of the CFA and VGA, the complicated PCAA method cannot trace the magnetic field in optically thick or thin media.

Furthermore, dust polarization is integrated along the line of sight and has limited applications (see Section 1). In contrast, the molecular line method is more suitable for locations that are along the line of sight. The current study shows that the VGT and CFA methods have ahigher accuracy than dust polarization in varying optical conditions and supports the scenario that the VGT has a huge potential for magnetic field tracing. Furthermore, it is noted that on the basis of the theoretical predictions of synchrotron emission fluctuations (Lazarian & Pogosyan 2012, 2016) confirmed by numerical simulations (Zhang et al. 2016; Zhang, Lazarian & Xiang 2018), synchrotron gradient techniques (Lazarian et al. 2017; Lazarian & Yuen 2018b; Zhang et al. 2019a; Zhang, Liu & Lazarian 2019b) and the quadrupole ratio of polarization intensities (Wang, Zhang & Xiang 2020), effective methods for measuring magnetic fields have been proposed and developed. Therefore, the synergetic applications of various techniques combined will significantly improve the quality of magnetic field measurements.

7 SUMMARY

Using a high-resolution numerical simulation, we have studied how to probe the direction of the mean magnetic field within the turbulent ISM using various molecular tracers. Based on the current understanding of MHD turbulence theory, CO and its isotopes are used as tracers to characterize the structures of anisotropic eddies. The orientation of the major axis of the eddies determines the direction of the mean magnetic field. The results obtained using

three techniques (VGT, CFA and PCAA) for tracing magnetic fields are summarized as follows.

The magnetic field directions can be recovered successfully using the VGT and CFA in the optically thick ISM. The AM performance of the VGT and CFA in the different optical depths of CO isotopologues becomes lower as the opacity decreases. The numerical results show that the AM slope using the VGT is flatter than that using CFA, indicating that the magnetic field tracing ability of the VGT is more stable than that of CFA.

The optical depth of CO isotopologues is proportional to their abundance: ^{12}CO/^{13}CO $\sim$ 50, ^{13}CO/C^{18}O $\sim$ 12. Compared with the dust polarization method, the VGT and CFA using the line-emission method have the potential to reveal the mean magnetic field directions reliably. Among them, ^{12}CO shows significant ability in magnetic field measurement. The ability of the PCAA technique for magnetic field tracing decreases compared with the other two techniques, in agreement with the earlier study without radiative transfer in Yuen et al. (2018).

DATA AVAILABILITY

The data underlying this article will be shared on reasonable request to the corresponding author.

REFERENCES

Andersson B.-G., Lazarian A., Vaillancourt J. E., 2015, ARA&A, 53, 501
Armstrong J. W., Rickett B. J., Spangler S. R., 1995, ApJ, 443, 209
Begum A., Chengalur J. N., Karachentsev I. D., Kaisin S. S., Sharina M. E., 2006, MNRAS, 365, 1220
Brunt C. M., Heyer M. H., 2002a, ApJ, 566, 276
Brunt C. M., Heyer M. H., 2002b, ApJ, 566, 289
Burkhart B., Stanimirović S., Lazarian A., Kowal G., 2010, ApJ, 708, 1204
Burkhart B., Lazarian A., Goodman A., Rosolowsky E., 2013, ApJ, 770, 141
Burkhart B., Lazarian A., Leão I. C., de Medeiros J. R., Esquivel A., 2014, ApJ, 790, 130
Chandran B. D. G., 2000, Phys. Rev. Lett., 85, 4656
Chen C.-Y., Ostriker E. C., 2014, ApJ, 785, 69
Chepurnov A., Lazarian A., 2010, ApJ, 710, 853
Cho J., Lazarian A., 2002, Phys. Rev. Lett., 88, 245001
Cho J., Vishniac E. T., 2000, ApJ, 539, 273
Deshpande A. A., Dwarakanath K. S., Goss W. M., 2000, ApJ, 543, 227
Dickey J. M., McClure-Griffiths N. M., Stanimirović S., Gaensler B. M., Green A. J., 2001, ApJ, 561, 264
Draine B. T., 2009, ASPC, 414, 453

Elmegreen B. G., Scalo J., 2004, ARA&A, 42, 211
Esquivel A., Lazarian A., 2005, ApJ, 631, 320
Esquivel A., Lazarian A., 2011, ApJ, 740, 117
Esquivel A., Lazarian A., Pogosyan D., 2015, ApJ, 814, 77
Federrath C., Chabrier G., Schober J., Banerjee R., Klessen R. S., Schleicher
    D. R. G., 2011, Phys. Rev. Lett., 107, 114504
Fermi E., 1949, Phys. Rev., 75, 1169
Fissel L. M. et al., 2019, ApJ, 878, 110
Galli D., Shu F. H., 1993, ApJ, 417, 220
Goldreich P., Sridhar S., 1995, ApJ, 438, 763
González-Casanova D. F., Lazarian A., 2017, ApJ, 835, 41
González-Casanova D. F., Lazarian A., 2019, ApJ, 874, 25
Green D. A., 1993, MNRAS, 262, 327
Hayes J. C. et al., 2006, ApJS, 165, 188
Heyer M., Gong H., Ostriker E., Brunt C., 2008, ApJ, 680, 420
Higdon J. C., 1984, ApJ, 285, 109
Hockney R. W., 1968, Phys. Fluids, 11, 1381
Hsieh C. H. et al., 2019, ApJ, 873, 16
Hu Y., Yuen K. H., Lazarian A., 2018, MNRAS, 480, 1333
Hu Y., Yuen K. H., Lazarian A., Fissel L. M., Jones P. A., Cunningham M.
    R., 2019, ApJ, 884, 137
Kandel D., Lazarian A., Pogosyan D., 2016, MNRAS, 461, 1227
Khalil A., Joncas G., Nekka F., Kestener P., Arneodo A., 2006, ApJS, 165,
    512
Kowal G., Lazarian A., 2010, ApJ, 720, 742
Larson R. B., 1981, MNRAS, 194, 809
Lazarian A. et al., 2018, ApJ, 865, 46
Lazarian A., 2006, AAS, 209, 17
Lazarian A., 2007, J. Quant. Spectrosc. Radiat. Transfer, 106, 225
Lazarian A., Pogosyan D., 2004, ApJ, 616, 943
Lazarian A., Pogosyan D., 2006, ApJ, 652, 1348
Lazarian A., Pogosyan D., 2012, ApJ, 747, 5
Lazarian A., Pogosyan D., 2016, ApJ, 818, 178
Lazarian A., Vishniac E. T., 1999, ApJ, 517, 700
Lazarian A., Yuen K. H., 2018a, ApJ, 853, 96
Lazarian A., Yuen K. H., 2018b, ApJ, 865, 59
Lazarian A., Pogosyan D., Esquivel A., 2002, in Taylor A. R., Landecker T.
    L., Willis A. G., eds, ASP Conf. Ser., Vol. 276, Seeing Through the Dust:
The Detection of HI and the Exploration of the ISM in Galaxies. Astron.
    Soc. Pac., San Francisco, p. 182
Lazarian A., Yuen K. H., Lee H., Cho J., 2017, ApJ, 842, 30
Lee H. M., Draine B. T., 1985, ApJ, 290, 211
Lithwick Y., Goldreich P., 2001, ApJ, 562, 279
Maron J., Goldreich P., 2001, ApJ, 554, 1175
McKee C. F., Ostriker E. C., 2007, ARA&A, 45, 565
Mestel L., Spitzer L., 1956, MNRAS, 116, 503
Montgomery D., 1982, Physica Scripta, 2A, 83
Mouschovias T. C., Spitzer L., 1976, ApJ, 210, 326
Myers P. C., Lazarian A., 1998, ApJ, 507, L157
Narayan R., Medvedev M. V., 2001, ApJ, 562, L129
Padoan P., Cambrésy L., Juvela M., Kritsuk A., Langer W. D., Norman M.
    L., 2006, ApJ, 649, 807
Schleicher D. R. G., Banerjee R., Sur S., Arshakian T. G., Klessen R. S., Beck
    R., Spaans M., 2010, A&A, 522, A115
Seifried D., Walch S., Reissl S., Ibáñez-Mejía J. C., 2019, MNRAS, 482,
    2697.
Vázquez-Semadeni E., Banerjee R., Gómez G. C., Hennebelle P., Duffin D.,
    Klessen R. S., 2011, MNRAS, 414, 2511
Wang R.-Y., Zhang J.-F., Xiang F.-Y., 2020, ApJ, 890, 70
Wilson C. D., Walker C. E., Thornley M. D., 1997, ApJ, 483, 210
Xu S., Lazarian A., 2020, ApJ, 890, 157
Xu S., Zhang B., 2016a, ApJ, 824, 113
Xu S., Zhang B., 2016b, ApJ, 832, 199
Yan H., Lazarian A., 2002, Phys. Rev. Lett., 89, 281102
Yan H., Lazarian A., 2008, ApJ, 673, 942
Yuen K. H., Lazarian A., 2017, ApJ, 837, L24
Yuen K. H. et al., 2018, ApJ, 865, 54
Zhang J.-F., Lazarian A., Lee H., Cho J., 2016, ApJ, 825, 154
Zhang J.-F., Lazarian A., Xiang F.-Y., 2018, ApJ, 863, 197
Zhang J.-F., Lazarian A., Ho K. W., Yuen K. H., Yang B., Hu Y., 2019a,
    MNRAS, 486, 4813
Zhang J.-F., Liu Q., Lazarian A., 2019b, ApJ, 886, 63

This paper has been typeset from a TEX/LATEX file prepared by the author.